This is an *Accepted Manuscript*, which has been through the RSC Publishing peer review process and has been accepted for publication.

Accepted Manuscripts are published online shortly after acceptance, which is prior to technical editing, formatting and proof reading. This free service from RSC Publishing allows authors to make their results available to the community, in citable form, before publication of the edited article. This *Accepted Manuscript* will be replaced by the edited and formatted *Advance Article* as soon as this is available.

To cite this manuscript please use its permanent Digital Object Identifier (DOI®), which is identical for all formats of publication.

More information about *Accepted Manuscripts* can be found in the **Information for Authors**.

Please note that technical editing may introduce minor changes to the text and/or graphics contained in the manuscript submitted by the author(s) which may alter content, and that the standard **Terms & Conditions** and the **ethical guidelines** that apply to the journal are still applicable. In no event shall the RSC be held responsible for any errors or omissions in these *Accepted Manuscript* manuscripts or any consequences arising from the use of any information contained in them.

A table of contents entry
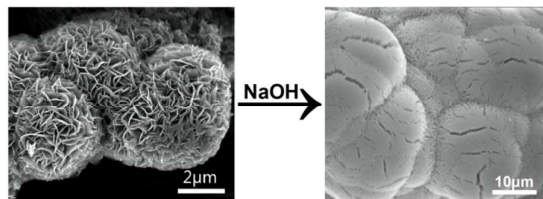
Hydrothermally synthesized MoS$_2$ products can be tuned from the porous flowers to the dense spheres by addition of NaOH.

Journal of
Materials Chemistry A

ARTICLE TYPE

Synthesis of Hierarchical MoS$_2$ and Its Electrochemical Performance as Anode Material for Lithium-Ion Batteries

Panling Sun, Wuxing Zhang,* Xianluo Hu, Lixia Yuan, and Yunhui Huang*

Received (in XXX, XXX) Xth XXXXXXXXX 20XX, Accepted Xth XXXXXXXXX 20XX

A facile process is developed to synthesize MoS$_2$ in the basic solution via a hydrothermal route by employing ammonium heptamolybdate and thiourea as starting materials and post-annealing in N$_2$ atmosphere at 450 °C for 5 h. The morphologies of the MoS$_2$ products can be tuned from the porous flowers to the dense spheres by addition of NaOH. Experimental results show that the MoS$_2$ products

10 have good crystallinity. The formation mechanism of the MoS$_2$ is proposed by that the dense MoS$_2$ spheres are evolved from the porous MoS$_2$ flowers through growing along the ⟨00l⟩ direction of the nano-sheets. Based on the growth mechanism, the microstructure of MoS$_2$ can be successfully controlled by adjustment of S/Mo ratio or addition of surfactant in the recipe. Electrochemical measurements demonstrate that the flower-like MoS$_2$ shows better electrochemical performance than MoS$_2$ spheres as

15 anode materials for Li-ion batteries, which delivers a high reversible capacity of 900 mA h g^{-1} at a current density of 100 mA g^{-1}, excellent cycling stability and rate capability.

Introduction

Lithium ion batteries (LIBs) have become the ubiquitous power sources in the portable electronic devices and have been

20 regarded as the most promising power sources for electric vehicles (EVs).[1] As for the anode materials in LIBs, graphite has been widely commercialized due to its natural abundance, flat potential profile versus lithium, high coulombic efficiency and structural stability during cycling. However, it cannot fully meet

25 the energy density requirement in EVs due to its relatively small theoretical specific capacity (372 mA h g^{-1}).[2,3] Therefore, alternative anode materials with higher specific capacity and good cycling behaviour are desirable for LIBs.

Recently, MoS$_2$ has attracted significant attention as the

30 anode material for LIBs. MoS$_2$ with stacked atom layers (S-Mo-S) held together by van der Waals force has demonstrated the interesting relationship between structure and properties, i. e., the weak van der Waals bonding between the basal planes is responsible for the lubrication properties,[4] while the faceted

35 edges control the catalytic properties.[5] Additionally, the layered structure of MoS$_2$ enables easy intercalation of metal ions, such as Li$^+$, Na$^+$ or Mg^{2+}, without obvious increase in volume.[6-9] When the first patent with MoS$_2$ as the electrode material in LIBs was published in 1980,[10] numerous studies on MoS$_2$ have been

40 conducted, especially as anode material for LIBs due to its large lithium storage capacity (theoretical 670 mA h g^{-1}) via a conversion reaction. Up to now, several methods have been developed to synthesize molybdenum sulfides, such as spray pyrolysis,[11] hydrothermal reaction,[12] evaporation method[13] and

45 precipitation method[14]. Accordingly, researchers have fabricated molybdenum sulfides with different morphologies such as nano-sheets[15], nano-tubes[16], nano-rods[12,17], flower-like particles and spheres[18,19]. It has been widely reported that MoS$_2$ with large surface area presents outstanding electrochemical performance,

50 suggesting that controllable synthesis of MoS$_2$ with large surface area is crucial to promote its application in LIBs.

Hydrothermal process is considered as an effective way to prepare inorganic nanomaterials due to such merits as mild synthetic conditions, simple manipulation, and good

55 crystallization of the products. It is quite interesting that the hydrothermal synthesized MoS$_2$ products are mainly nano-sheets and flower-like spheres due to its intrinsic tabular growth habit arising from the layered structure[9,20-23]. Thus, the morphology control of MoS$_2$ during the hydrothermal synthesis has attracted

60 extensive attention. Variable hierarchical MoS$_2$ microstructures have been achieved via adding surfactant and acid in the hydrothermal reaction. Li et al. synthesized flower-like MoS$_2$ hollow microspheres by a facile hydrothermal route with the assistance of Pluronic F-127.[21] Wang et al. hydrothermally

65 produced amorphous MoS$_2$ nano-spheres by adding hydroxylamine hydrochloride.[24] MoS$_2$ nano-rods and nano-fibers were successfully synthesized via hydrothermal method by adding acidic additives.[12,25] The additives of surfactant and acid are supposed to affect the sulfureted reaction or reduction

70 reaction during the multi-step formation of MoS$_2$, and result in the morphology changes.

Formation of MoS$_2$ in the basic condition has been seldom reported. Recently, Mitra et al. synthesized the flower-like MoS$_2$

in the ammonium solution and suggest that excessive OH$^-$ ions have blocking effect on ⟨001⟩ direction to form a lamellar structure.[26] Herein, we also report a facile process to synthesize MoS$_2$ in the basic solution via a hydrothermal route by employing
5 ammonium heptamolybdate and thiourea as starting materials. It was found that the morphology of the products can be tuned from the porous flowers to the dense spheres by addition of NaOH. The formation mechanism of MoS$_2$ spheres in the basic condition has been explored. As anode material for LIBs, the obtained
10 flower-like MoS$_2$ exhibits high specific capacity, enhanced cycling stability and excellent rate capability.

Experimental Section

Synthesis

All reagents are of analytical grade without further
15 purification. Thiourea (N$_2$H$_4$CS) was dissolved in NaOH solution (0–5 mol l^{-1}) and followed by addition of ammonium heptamolybdate. The concentration of ammonium heptamolybdate was kept constant at 0.5 mol l^{-1} while thiourea was in 10% excess of the stoichiometric amount. The
20 hydrothermal reaction was carried out in Teflon-lined stainless autoclave at 220 °C for 10 h. The obtained black precipitate was collected by centrifuge, washed by distilled water and ethanol, and dried at 80 °C. The dried precipitate was annealed at 450 °C for 5 h in N$_2$ atmosphere. The MoS$_2$ samples prepared in different
25 NaOH concentration were marked with MS-xM, where x represents the concentration of NaOH.

Characterizations

The morphologies of the samples were observed by scanning electron microscope (SEM, FEI, Sirion 200). The structures were
30 checked by X-ray diffraction (XRD, X'Pert PRO, PANalytical B.V., Holland diffractometer employing a Cu-K$_{\alpha 1}$ source, λ = 1.5406 Å) and high-resolution transmission electron microscopy (HRTEM, JEOL JEM-2010). The samples for HRTEM measurement were prepared on the standard holey carbon
35 covered copper micro-grid.

Electrochemical measurements

The electrochemical tests were carried out in CR2032 coin cells. MoS$_2$ was used as working electrode, lithium foils as counter and reference electrode, polypropylene film (Celgard-
40 2300) as separator, and 1 mol l^{-1} LiPF$_6$ dissolved in a mixture of ethylene carbonate and dimethyl carbonate (EC/DMC, 1:1 in volume) as electrolyte. The working electrodes were prepared by a slurry tape casting procedure. The slurry consisted of 80 wt% active materials, 10 wt% acetylene black (Super-P) and 10 wt%
45 polyvinylidene fluoride (PVDF) dissolved in N-methyl-2-pyrrolidinone (NMP). The slurry was tape-casted on the copper foil, the current collector. The coated electrodes were dried at 80 °C for 24 h in vacuum, and then assembled into coin cells in an argon-filled glove box. Cyclic voltammetry measurements were
50 performed on an electrochemical workstation (PARSTAT 2273) at a scan rate of 0.5 mV s^{-1} over the potential range of 0.01–3.0 V (vs. Li$^+$/Li). The galvanostatic charge/discharge tests were conducted on the battery measurement system (LAND CT2001A, China) at various current densities of 100–1000 mA g^{-1} with a
55 cutoff voltage range of 3.00–0.01 V vs. Li/Li$^+$ at room temperature. Alternating current impedance spectra were obtained

by applying a sine wave with amplitude of 0.5 mV over the frequency range from 200 kHz to 0.01 kHz.

Results and Discussion

60 Figure 1 shows the XRD patterns of the MoS$_2$ calcined at 450 °C for 5 h in N$_2$ atmosphere. Thermal evolution of the hydrothermally sythesized MoS$_2$ has been systematically investigated by Bokhimi et al.,[27] which demonstrates that post
65 annealing is helpful to remove the hydroxyls on the particle surface and improve the crystallization. XRD and TG results also prove the improvement of crystallization (Fig. S1 and S2). It is clear that all the calcined samples are congruent with a hexagonal structure of MoS$_2$ (JCPDS 37-1492), in which the diffraction
70 peaks at 2θ = 14, 33, 39 and 59.8 can be unambiguously assigned to the (002), (100), (103) and (110) planes, respectively. No obvious peaks from impurity phase are observed in the XRD patterns. The sharp (002) peak indicates the formation of well-stacked layer structure of MoS$_2$.
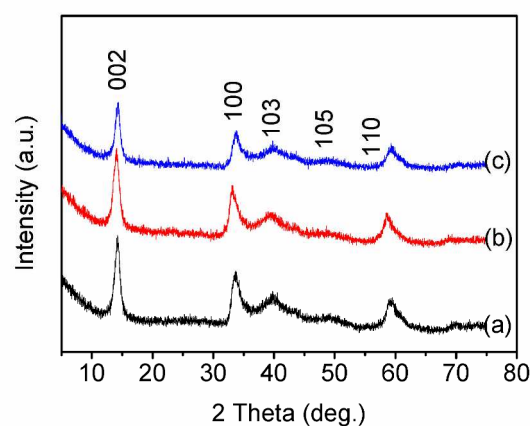
75 **Fig. 1** XRD patterns of MoS$_2$ synthesized in different NaOH concentration and calcined at 450 °C for 5 h in N$_2$ atmosphere. (a) MS-0M; (b) MS-1M; (c) MS-3M.
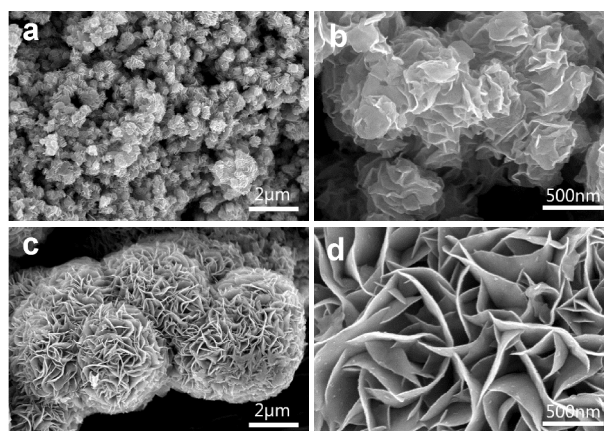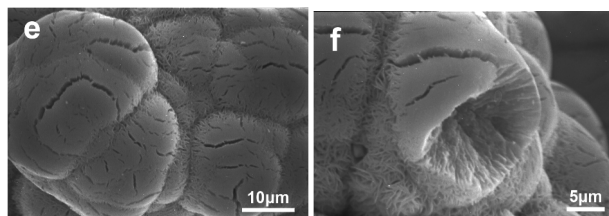
Fig. 2 SEM images of the as prepared MoS_2 in different NaOH concentration. (a, b) MS-0M; (c, d) MS-1M; (e, f) MS-3M.

Figure 2 shows the SEM images of MoS_2 synthesized in different NaOH concentration at 220 °C for 10 h. It can be seen that all the MoS_2 samples show a hierarchical structure. The sample without addition of NaOH consists of many secondary fine particles made up of ultrathin nanosheets with mean diameter of ca. 500 nm (Fig. 2a, b). With small addition of NaOH, the morphology of MoS_2 greatly changes (Fig. S3). In 1 mol l^{-1} NaOH solution, flower-like MoS_2 particles are obtained (MS-1M, Fig. 2c, d); whereas in 3 mol l^{-1} NaOH solution, agglomerated spheres with size of 5–10 μm are formed (MS-3M, Fig. 2e). Close view of the spherical particles shows that the MoS_2 spheres are quite dense, which are connected by porous nanosheets-based texture (Fig. 2f). If NaOH concentration is higher than 4 mol l^{-1}, no product is formed. HRTEM images of the flower-like particles clearly display the typical interlayer structure of MoS_2, and the fringe distance of the interlayer is calculated to be 6.9 Å, corresponding to the spacing between (002) basal planes of MoS_2 (Fig. 3). BET results show that the calcined MS-0M, MS-1M and MS-3M have the specific surface area of 13.2, 9.2 and 5.9 m^2/g, respectively.
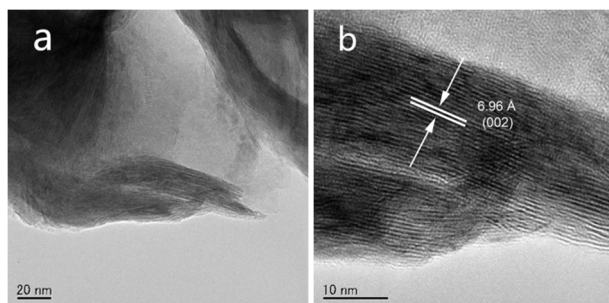
Fig. 3 TEM images of the MoS_2 as prepared in 1 mol l^{-1} NaOH solution.

It has been reported that Mo(VI) ions exist in the form of MoO_4^{2-} in the basic solution.[28] During the formation of sulfide, thiourea acts as sulfur source and reducing reagent, and the hydrolysis of thiourea can be accelerated in the basic medium.[29,30] Furthermore, the solubility of MoS_2 increases with increasing basicity,[28] which results in the decreasing yield of MoS_2. If NaOH concentration is up to 4 mol l^{-1}, all the MoS_2 particles can be dissolved in the solution and no product can be obtained. Thus, the possible reactions for the formation of MoS_2 in basic solution can be expressed as:

$$(NH_2)_2SC + OH^- \rightarrow S^{2-} + CH_2N_2 + H_2O \qquad (1)$$

$$MoO_4^{2-} + S^{2-} \rightarrow MoS_2 + SO_4^{2-} \qquad (2)$$

$$MoS_2 + O_2 + OH^- \rightarrow MoO_4^{2-} + SO_4^{2-} + H_2O \qquad (3)$$
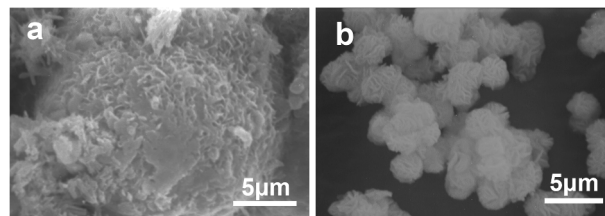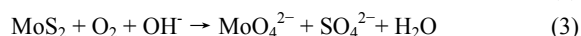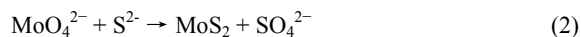
Fig. 4 SEM images of the MoS_2 particles as synthesized in different reaction conditions. (a) 1 mol l^{-1} NaOH, 220 °C for 48 h; (b) 3 mol l^{-1} NaOH, 220 °C for 1 h.

The flower-like MoS_2 is formed from the agglomerated nuclei accompanied by the atomic sulfur substitution of oxygen.[31] Due to the laminar growth habit of the molybdenum sulfide, the agglomerated nuclei grow into flower-like microstructure. In our experiments, the particle size in basic solution is much larger than that without addition of NaOH. Similar results were obtained by using ammonium solution as the basic medium (Fig. S4).[26] This can be ascribed to the accelerated hydrolysis of thiourea into S^{2-} in the basic medium. Furthermore, it is observed that the flower-like particles formed in 1 mol l^{-1} NaOH are transformed into dense spherical structure by elongate the reaction time to 48 h (Fig. 4a), while the particles formed in 3 mol l^{-1} NaOH solution are flower-like if the reaction time is shortened to 1 h (Fig. 4b). Therefore, it can be concluded that the sphere-like MoS_2 is evolved from the flower-like structure.
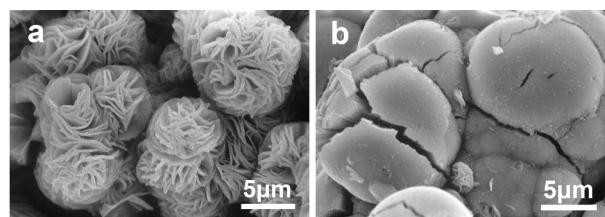
Fig. 5 SEM images of the samples as obtained in 3 mol l^{-1} NaOH solution at 220 °C for 10 h: (a) with EDTA·2Na, S/Mo ratio = 2.2; (b) without EDTA·2Na, S/Mo ratio = 3.

The above formation mechanism of MoS_2 in the hydrothermal reaction indicates that if the growth along $\langle 00l \rangle$ direction is suppressed, the product is apt to form flower-like structure; otherwise, dense spheres can be obtained. To further prove this, ethylenediaminetetraacetic acid disodium salt (EDTA·2Na) is used as a surfactant to inhibit the growth along $\langle 00l \rangle$ direction since EDTA is a strong chelating agent.[32] Interestingly, the morphology of MoS_2 product is totally different with and without EDTA. SEM images in Fig. 5 show that flower-like particles are achieved with EDTA whereas dense spheres are formed without EDTA (Fig.2e and f). EDTA capped at the surface can block the sulfur bonding. Without EDTA, abundant sulfur can be supplied for reaction. The capping effect of surfactant was also found for CTAB, F-127 and SDBS in the formation of flower-like MoS_2.[21] In addition, it is observed that the agglomerated spheres show a denser structure even at the connection area if the S/Mo ratio is increased to 3 (Fig. 5b), which indicates that the growth along $\langle 00l \rangle$ direction is accelerated. As shown in XRD patterns in Fig. 6, after annealing at 450 °C for 5 h in N_2, the flower-like particles obtained at presence of EDTA show the impurity phase of MoO_2, demonstrating the suppressed sulfur substitution of oxygen in the

nuclei. With no EDTA, pure MoS_2 with spherical morphology is obtained since enough sulfur is released to react with Mo ions. Therefore, the phase purity and the morphology of MoS_2 can be effectively controlled by tuning the growth rate along $\langle 00l\rangle$

5 direction.
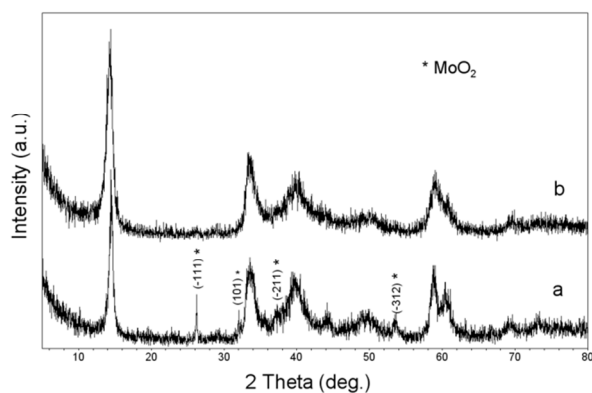
Fig. 6 XRD patterns of the samples annealed at 450 °C for 5 h in N_2, formed in 3 mol l^{-1} NaOH solution at 220 °C for 10 h as precursors: (a) with EDTA·2Na, S/Mo ratio = 2.2; (b) without EDTA·2Na, S/Mo ratio =
10 3.
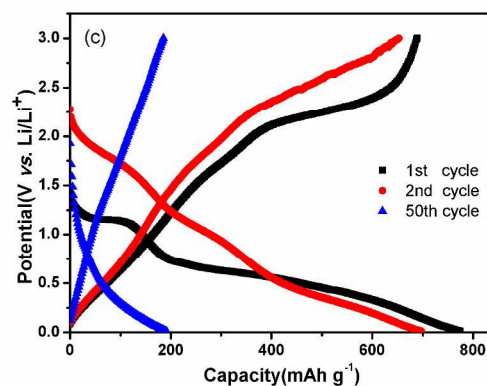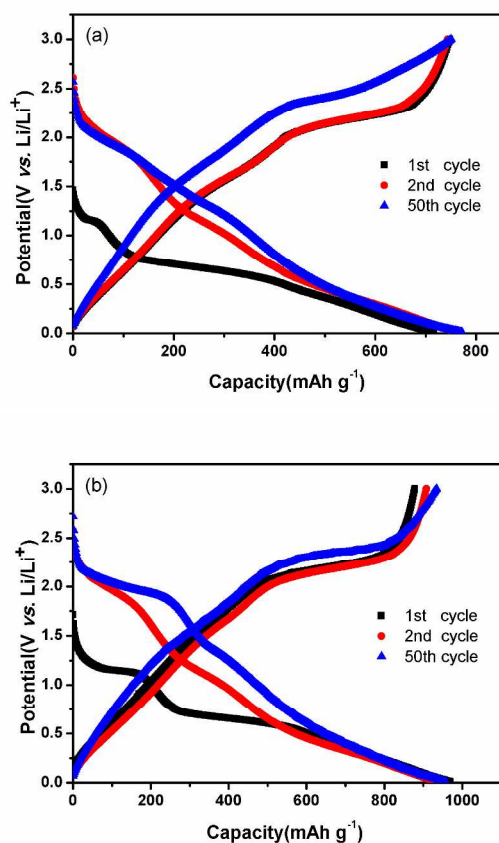
Fig. 7 Charge and discharge curves for different MoS_2 electrodes at a
15 current density of 100 mA g^{-1} in the voltage range of 0.01–3 V (vs. Li/Li$^+$): (a) MS-0M; (b) MS-1M; (c) MS-3M.

The hierarchical MoS_2 samples are investigated as anode materials for LIBs. Fig. 7 illustrates the charge/discharge voltage profiles of MoS_2 obtained in different NaOH concentration
20 measured at a current density of 100 mA g^{-1} in the voltage range of 0.01–3 V (vs. Li/Li$^+$). As shown in Fig. 7a, during the first discharge (lithiation process), two potential plateaus appear at around 1.2 and 0.6 V, which can be attributed to the phase formation of Li_xMoS_2 and the subsequent reduction of Mo^{4+} to
25 Mo nanoparticles embedded in Li_2S matrix, respectively.[33] The overall reaction can be described as: $MoS_2 + 4Li^+ + 4e^- \rightarrow Mo + 2Li_2S$. In the 2nd and 50th discharge curves, the potential plateau at ∼0.6 V disappears, and two new potential plateaus appear at ∼1.9 and 1.4 V, which may correspond to the redox reaction of
30 Li_2S/S in a deeply discharged MoS_2/Li cell according to Wang's reports.[33,34] Upon the charge process (delithiation), two plateaus at ∼1.7 V and 2.2 V can be clearly identified for the 1st and subsequent cycles, indicative of the lithium extraction process from Li_2S. Fig. 7b shows that the MS-1M electrode displays
35 obvious potential plateaus at 1.2 and 0.6 V in the first discharge and at 1.7 and 2.2 V in the first charge process. These results are in accordance with those obtained without NaOH. However, the potential plateaus become inconspicuous for MS-3M. The initial discharge capacities of the MS-0M, MS-1M and MS-3M
40 electrodes are 740, 980 and 760 mA h g^{-1}, respectively, while their initial charge capacities are 730, 900 and 720 mA h g^{-1}. Among these electrodes, MS-1M exhibits the highest lithiation and delithiation capacities. The irreversible capacity loss in the 1st cycle can be mainly attributed to the irreversible processes
45 including the electrolyte decomposition and inevitable formation of the solid-electrolyte interface (SEI) layer, which are common for the nanostructured anode materials.[35]

To further clarify the electrochemical process of MoS_2, cyclic voltammogram (CV) measurements are carried out. Fig. 8 depicts
50 the CV curves of different MoS_2 electrodes in the voltage range of 3−0.01 V at a scan rate of 0.5 mV s^{-1}. In the first cycle of MS-0M, two reduction peaks are observed at 0.9 V and 0.4 V, in which the reduction peak at 0.9 V can be attributed to the Li insertion into MoS_2, and the peak at 0.4 V to the reduction of
55 Li_xMoS_2 to Mo and Li_2S via a conversion reaction, accompanied by the formation of SEI film and electrolyte decomposition. The

oxidation peaks at 1.8 V and 2.3 V correspond to the delithiation from Li_2S.[33,34] In the subsequent discharge cycles, the reduction peaks observed at 0.4 V and 0.9 V are replaced by two new peaks at 1.9 V and 1.2 V. The significant difference of the CV plots between the 1st and subsequent discharges is in agreement with the previous observation in the literature, indicating that MoS_2 experiences an irreversible phase transition in the initial discharge.[36] As shown in Fig. 8b, MS-1M electrode demonstrates the similar peak position to MS-0M. However, the oxidation and reduction peaks of MS-3M almost disappear in the subsequent cycles, which agree well with the previous charge/discharge profiles. It is obvious that MS-3M with dense structure exhibits much degraded electrochemical activity and reversibility for Li^+ storage.

The cycling behaviour of the MoS_2 samples at a current density of 100 mA g^{-1} between 0.01–3 V is shown in Fig. 9a. It is obvious that MS-3M presents the poorest cyclic stability since the reversible capacity decreases to 186 mA h g^{-1} after 50 cycles, only 25.8% of the initial capacity. On the contrary, the reversible capacity of MS-1M maintains at 957 mA h g^{-1} after 50 cycles. However, the capacities of MS-1M and MS-0M begin to decrease after 60th cycles, and finally approach the capacity of MS-3M. Generally, flower-like MS-1M and MS-0M exhibit superior cycling performance than that of spherical MS-3M because the flower-like MS-1M and MS-0M can relieve the structure change better than MS-3M during the conversion reaction. The cycling performance of MS-1M may be further improved after carbon coating. Fig. 9b shows the rate cycling behaviour of MoS_2 at various current densities. It is seen that MS-1M also demonstrates the best rate performance. The specific capacity remains at ~800 mA h g^{-1} even at a high current density of 1000 mA g^{-1}.
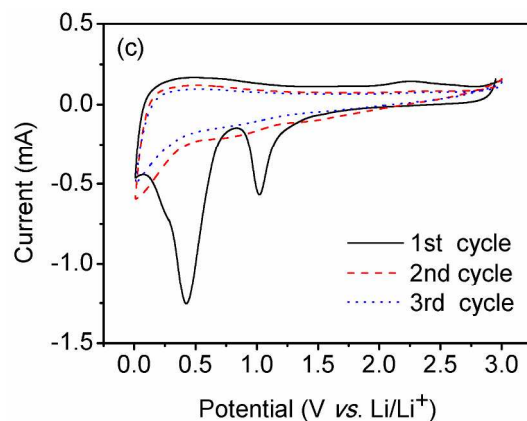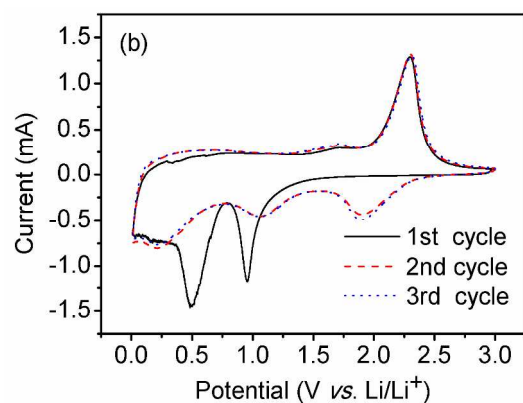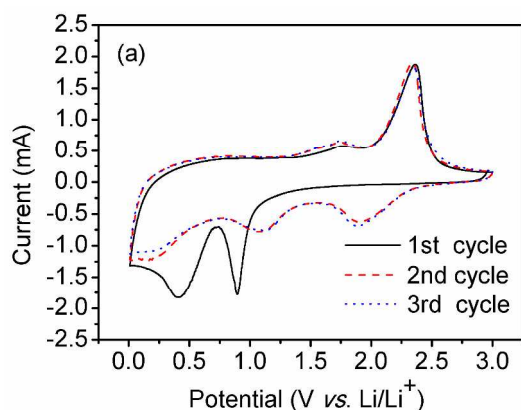
Fig. 8 Cyclic voltammetry curves (initial three cycles) of different MoS_2 samples measured at a scan rate of 0.5 mV s^{-1} in the voltage range of 0.01–3 V (vs. Li/Li^+): (a) MS-0M; (b) MS-1M; (c) MS-3M.

To further understand the different electrochemical performance of MoS_2, EIS measurements are conducted after 5 cycles (Fig. 10). MS-1M electrode shows the smallest radius of semi-circle in the Nyquist plots, suggesting a low contact and charge-transfer resistance in the MS-1M electrode. The enhanced conductivity facilitates the electron and Li^+ ion transfer in the electrode. Comparatively, the MS-3M shows large contact and charge-transfer resistances due to its dense structure. Considering the low specific surface area of the MoS_2 products, it indicates that the hierarchical structure constructed by nano-blocks is effective to improve the electrochemical performance of micron-sized MoS_2. The ultrathin nanosheets in MS-1M shorten the diffusion path of Li^+ ions. The large lateral size of the nanosheets in MS-1M also provides large contact area between MoS_2 and electrolyte, which offers more active sites for Li^+ insertion/distraction, resulting in high specific capacity. Furthermore, the voids between the nanosheets can effectively mitigate the stress to protect the active materials from pulverization during the lithiation/delithiation process. Therefore, the cycling and rate performance of the MS-1M is greatly enhanced.
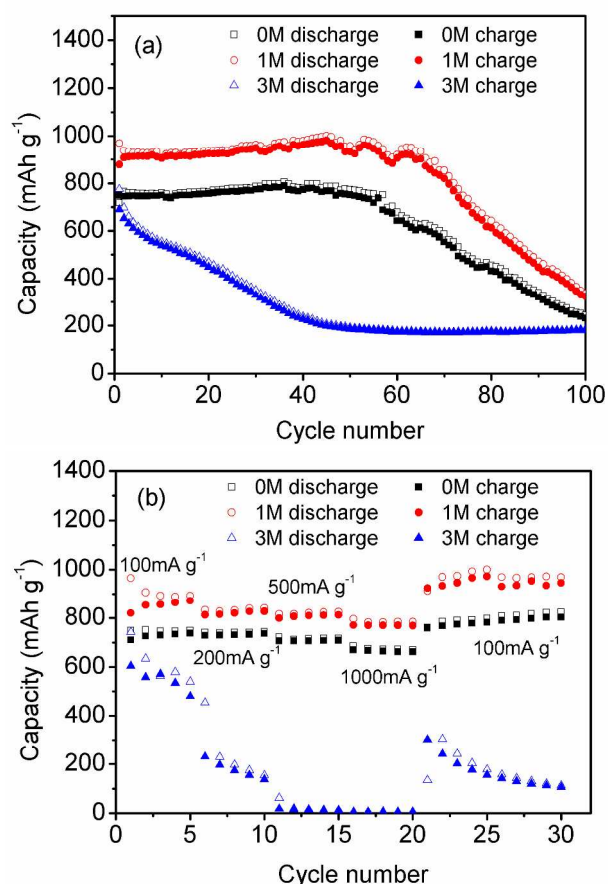
Fig. 9 (a) Cycling performance for different MoS_2 electrodes at a current density of 100 mA h g^{-1} in the voltage range of 0.01–3 V (vs. Li/Li$^+$); (b) rate performance of the different MoS_2 electrodes.
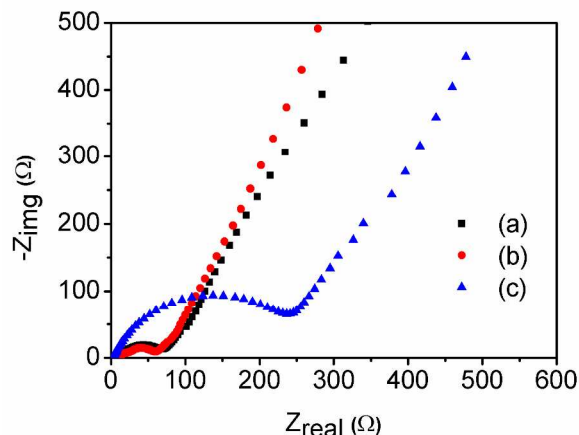
Fig. 10 Nyquist plots of the different MoS_2 electrodes in the frequency range from 200 kHz to 0.01 kHz. (a) MS-0M; (b) MS-1M; (c) MS-3M.

Conclusions

A facile hydrothermal route is successfully developed to synthesize hierarchical MoS_2 in the basic solution. Flower-like MoS_2 is formed in 1 mol l^{-1} NaOH solution, while spherical MoS_2 is obtained in 3 mol l^{-1} NaOH. XRD and HRTEM show that the MoS_2 samples are well crystallized after annealing in N_2 atmosphere at 450 °C for 5 h. SEM images demonstrate that the flower-like MoS_2 firstly forms in the hydrothermal reaction and then grows into dense MoS_2 spheres. Based on the growth mechanism, the morphology of MoS_2 can be effectively controlled by adjusting S/Mo ratio or addition of EDTA·2Na as surfactant. Electrochemical measurements demonstrate that the flower-like MoS_2 made up of nanosheets shows the highest reversible capacity of 900 mA h g^{-1} at a current density of 100 mA g^{-1} with minor capacity fading over 50 cycles. Even at a high current density of 1000 mA g^{-1}, the specific capacity retains at 800 mA h g^{-1}. As a comparison, the dense MoS_2 spheres obtained in 3 mol l^{-1} NaOH solution display lower specific capacity, poorer cyclic stability and worse rate performance. EIS analysis confirms the high conductivity of MS-1M, which greatly enhances electrochemical reaction kinetics. The excellent electrochemical performance of flower-like MoS_2 particles with micron size is attributed to the hierarchical structure made up of nanosheets. Our results prove that MoS_2 with hierarchical structure holds promise as anode material for high-performance LIBs.

Notes and references

State Key Laboratory of Materials Processing and Die & Mould Technology, School of Materials Science and Engineering, Huazhong University of Science and Technology, Wuhan 430074, China

E-mail: zhangwx@mail.hust.edu.cn; huangyh@mail.hust.edu.cn

1   J. B. Goodenough and K. S. Park, *J. Am. Chem. Soc.*, 2013, **135**, 1167-1176.

2   K. Kang, Y. S. Meng, J. Bréger, C. P. Grey and G. Ceder, *Science*, 2006, **311**, 977-980.

3   F. Y. Cheng, J. Liang, Z. L. Tao and J. Chen, *Adv. Mater.*, 2011, **23**, 1695-1715.

4   J. Kogovšek, M. Remškar, A. Mrzel and M. Kalin, *Tribol. Int.*, 2013, **61**, 40-47.

5   Y. G. Li, H. L. Wang, L. M. Xie, Y. Y. Liang, G. S. Hong and H. J. Dai, *J. Am. Chem. Soc.*, 2011, **133**, 7296-7299.

6   K. Chang and W. X. Chen, *ACS Nano*, 2011, **5**, 4720-4728.

7   J. Park, J. S. Kim, J. W. Park, T. H. Nam, K. W. Kim, J. H. Ahn, G. X. Wang and H. J. Ahn, *Electrochim. Acta*, 2013, **92**, 427-432.

8   X. L. Li and Y. D. Li, *J. Phy. Chem. B*, 2004, **108**, 13893-13900.

9   Y. C. Liu, L. F. Jiao, Q. Wu, J. Du, Y. P. Zhao, Y. C. Si, Y. J. Wang and H. T. Yuan, *J. Mater. Chem. A*, 2013, **1**, 5822-5826.

10   R. R. Haering, J. A. R. Stiles and K. Brandt, US Patent 4224390, 1980.

11   S. E. Skrabalak and K. S. Suslick, *J. Am. Chem. Soc.*, 2005, **127**, 9990-9991.

12   H. T. Lin, X. Y. Chen, H. L. Li, M. Yang and Y. X. Qi, *Mater. Lett.*, 2010, **64**, 1748-1750.

13   A. Zak, Y. Feldman, V. Alperovich, R. Rosentsveig and R. Tenne, *J. Am. Chem. Soc.*, 2000, **122**, 11108-11116.

14   K. H. Hu, Y. R. Wang, X. G. Hu and H. Z. Wo, *Mater. Sci. Technol.*, 2007, **23**, 242-246.

6 | *J. Mater. Chem. A*, 2013, **[vol]**, 00–00

This journal is © The Royal Society of Chemistry 2013

15   X. S. Zhou, L. J. Wan and Y. G. Guo, *Chem. Commun.*, 2013, **49**, 1838-1840.

16   M. Remskar, A. Mrzel, Z. Skraba, A. Jesih, M. Ceh, J. Demšar, P. Stadelmann, F. Lévy, D. Mihailovic, *Science*, 2001, **292**, 479-481.

17   Y. M. Tian, J. Z. Zhao, W. Y. Fu, Y. H. Liu, Y. Z. Zhu and Z. C. Wang, *Mater. Lett.*, 2005, **59**, 3452-3455.

18   P. Afanasiev and I. Bezverkhy, *Chem. Mater.*, 2002, **14**, 2826-2830.

19   S. J. Ding, D. Y. Zhang, J. S. Chen and X. W. Lou, *Nanoscale*, 2012, **4**, 95-98.

20   Y. D. Liu, L. Ren, X. Qi, L. W. Yang, G. L. Hao, J. Li, X. L. Wei and J. X. Zhong, *J. Alloys Comp.*, 2013, **571**, 37-42.

21   G. G. Tang, Y. J. Wang, W. Chen, H. Tang and C. S. Li, *Mater. Lett.*, 2013, **100**, 15-18.

22   S. K. Park, S. H. Yu, S. Woo, B. Quan, D. C. Lee, M. K. Kim, Y. E. Sung and Y. Z. Piao, *Dalton Trans.*, 2013, **42**, 2399-2405.

23   W. J. Zhou, Z. Y. Yin, Y. P. Du, X. Huang, Z. Y. Zeng, Z. X. Fan, H. Liu, J. Y. Wang and H. Zhang, *Small*, 2013, **9**, 140-147.

24   Y. M. Tian, X. Zhao, L. C. Shen, F. Y. Meng, L. Q. Tang, Y. H. Deng and Z. C. Wang, *Mater. Lett.*, 2006, **60**, 527-529.

25   G. Nagaraju, C. N. Tharamani and G. T. Chandrappa, *Nanoscale Res. Lett.*, 2007, **2**, 461-468.

26   U. K. Sen and S. Mitra, *ACS Appl. Mater. Interfaces*, 2013, **5**, 1240-1247.

27   X. Bokhimi, J. A. Toledo, J. Navarrete, X. C. Sun and M. Portilla, *Int. J. Hydrogen Energy*, 2001, **26**, 1271-1277.

28   N. Yamasaki, S. Kanahara and K. Yanagisawa, *Chem. Soc. Jp*, 1985, **1**, 141-143.

29   F. Göede, C. Güemües and M. Zor, *J. Cryst. Growth*, 2007, **299**, 136-141.

30   T. Ben Nasr, N. Kamoun and C. Guasch, *Mater. Chem. Phys.*, 2006, **96**, 84-89.

31   R. H. Wei, H. B. Yang, K. Du, W. Y. Fu, Y. M. Tian, Q. J. Yu, S. K. Liu, M. H. Li and G. T. Zou, *Mater. Chem. Phys.*, 2008, **108**, 188-191.

32   Y. H. Ma, L. Han, K. Miyasaka, P. Oleynikov, S. Che and O. Terasaki, *Chem. Mater.*, 2013, **25**, 2184-2191.

33   X. P. Fang, C. X. Hua, X. W. Guo, Y. S. Hu, Z. X. Wang, X. P. Gao, F. Wu, J. Z. Wang and L. Q. Chen, *Electrochim. Acta*, 2012, **81**, 155-160.

34   X. P. Fang, X. W. Guo, Y. Mao, C. X. Hua, L. Y. Shen, Y. S. Hu, Z. X. Wang, F. Wu and L. Q. Chen, *Chem. Asian J.*, 2012, **7**, 1013-1017.

35   W. H. Shi, J. X. Zhu, X. H. Rui, X. H. Cao, C. Chen, H. Zhang, H. H. Hng and Q. Y. Yan, *ACS Appl. Mater. Interfaces*, 2012, **4**, 2999-3006.

36   X. H. Cao, Y. M. Shi, W. H. Shi, X. H. Rui, Q. Y. Yan, J. Kong and H. Zhang, *Small*, 2013, DOI: 10.1002/smll.201202697

Journal of Materials Chemistry A Accepted Manuscript